INORGANIC CHEMISTRY
FRONTIERS

RESEARCH ARTICLE

View Article Online
View Journal | View Issue

Cite this: *Inorg. Chem. Front.*, 2025, **12**, 2881

Nanometer-sized nickel and cobalt doped forsterite synthesis for investigating critical element recovery from mafic and ultramafic rocks†

Kelly A. Peterson, *[a] Mark E. Bowden, [a] Bavan P. Rajan, [a] Tenley E. Webb,[a] Bridgette N. Carven,[a] Libor Kovarik, [a] Zsombor Molnár,[a] Mark H. Engelhard, [b] Sandra D. Taylor, [a] Elsa A. Cordova,[b] Thomas W. Wietsma,[c] Sebastian T. Mergelsberg, [a] Christopher J. Thompson, [b] Sebastien N. Kerisit [a] and John S. Loring *[a]

Received 13th October 2024,
Accepted 18th February 2025

DOI: 10.1039/d4qi02586e

rsc.li/frontiers-inorganic

A synthesis method for nanosized forsterite (Mg_2SiO_4) doped with varying concentrations of Ni and Co has been developed to support studies of carbonation-based extraction and separation of Ni and Co from mafic and ultramafic rocks. The protocol expands upon an existing sol–gel/surfactant method and is demonstrated for doping levels of 5% and 25% of Ni or Co. Variables such as metal reagents, surfactant ratios, and calcination procedures were optimized to achieve high specific surface areas and small particle sizes while minimizing secondary phase formation. Particle sizes ranged from 29 to 83 nm, and specific surface areas were between 11 and 32 $m^2\ g^{-1}$. Metal oxide impurities were minimal, appearing only in undoped and 25% Ni-doped samples at 0.6 wt% or less. Ni and Co were only detected in the +II oxidation state and partitioned predominantly in the M1 cation site of the forsterite crystal structure. Doped nanosized forsterites prepared with this method will enable *in situ* experiments that can track, at the molecular scale, the fate of Ni and Co during carbonation reactions and thus provide a knowledge base for improving metal extraction and separation technologies.

1. Introduction

Nickel and cobalt are widely used in the manufacture of rechargeable batteries and alloys.[1–3] Both are critical components of lithium-ion batteries, and the rapid growth in electric vehicles has caused increased production and rising costs for both elements. Demand has been predicted to exceed production for Ni by 2037 and for Co by 2030 or sooner.[4] Many of the world's largest economies, including the United States and the European Union, have designated Ni and Co as critical or strategic minerals/raw materials based on concerns about supply chain disruptions from a limited number of foreign sources.[1,5,6] The primary source of Co is the Democratic Republic of the Congo, with 74% of world production, and Ni production is dominated by a small group of nations: Indonesia, the Philippines, Canada, New Caledonia, Russia, and Australia.[4] Consequently, there is a strong motivation to develop alternate supplies for both elements.

Mafic and ultramafic rocks, comprised of divalent metal silicate minerals rich in Mg, Fe, and Ca, can also contain Ni and Co at concentrations in the 100's to 1000's of ppm.[7,8] These rocks are considered low-grade ores by the mining industry, yet they are abundant and offer high potential for durable CO_2 storage.[9,10] Carbonating these rocks could improve the economic viability of Ni and Co extraction by lowering processing costs and helping the mining industry reach net-zero CO_2 emissions. Researchers are actively developing methods to separate and recover Ni and Co from mafic and ultramafic ores *via* carbonation, including precipitating these metals as sulfides or selectively complexing them in solution using organic ligands.[11–15] To better understand and optimize separation and recovery methods, there is a need for model silicate minerals with known quantities of Ni and/or Co. Moreover, these methods would greatly benefit from mechanistic studies of carbonation; however, such studies rely on *in situ* monitoring of carbonation reactions on laboratory time-

[a]*Physical and Computational Sciences Directorate, Pacific Northwest National Laboratory, Richland, WA 99352, USA. E-mail: kelly.peterson@pnnl.gov, john.loring@pnnl.gov*
[b]*Energy and Environment Directorate, Pacific Northwest National Laboratory, Richland, WA 99352, USA*
[c]*Earth and Biological Sciences Directorate, Pacific Northwest National Laboratory, Richland, WA 99352, USA*
† Electronic supplementary information (ESI) available. See DOI: https://doi.org/10.1039/d4qi02586e

scales (*e.g.*, hours to a few days), using techniques such as infrared spectroscopy[16–18] and X-ray diffraction[19–21] that require materials with high specific surface area only achievable by nanosized particles. Therefore, synthesizing nanosized divalent metal silicates with controlled amounts of Ni or Co is key to exploiting the potential benefits of Ni and Co recovery from mafic and ultramafic rocks.

Forsterite (Mg_2SiO_4), the Mg endmember of the olivine group, is an important component of mafic and ultramafic rocks that has been used to study carbonation of silicate minerals.[16–18,20–30] Forsterite can be synthesized in nanosized form with the high specific surface area and high purity needed for *in situ* experimental research. For example, Sanosh *et al*. calcined an aged aqueous sol–gel containing magnesium nitrate and tetraethylorthosilicate to produce forsterite particles between 5–90 nm, with an average of 27 nm.[31] In previous carbonation studies from our group,[16–18,23–25] forsterites were synthesized from a precursor gel containing polyvinyl alcohol and a sucrose template.[32–34] This synthesis yielded nanosized forsterite with estimated crystallite sizes of 24 nm, specific surface area of 42.3 $m^2\ g^{-1}$, and 1.3 wt% MgO.[32] Anovitz *et al*. reported an anhydrous sol–gel/surfactant synthesis using magnesium methoxide to produce nano-scale forsterite with specific surface area up to 76.6 $m^2\ g^{-1}$ and no other phases detected.[35]

Several techniques have been reported for synthesizing transition metal-doped forsterites, including solid-state,[36,37] solvothermal,[38] sol–gel,[39,40] and mechanochemical methods.[41] However, none of these approaches produce materials with the purity and specific surface area suitable for *in situ* experimental studies. For example, El Hadri *et al*. utilized a combined sol–gel and hydrothermal method to produce Ni- or Co-doped forsterites with average aggregate sizes ranging from 0.1 to 5 μm.[39] Tena *et al*. synthesized Ni- and Co-doped forsterites using a co-precipitation method, yielding average particle sizes of 353 to 699 nm. However, some of these forsterites were accompanied by secondary phases such as MO (M = Ni, Co), Co_3O_4, or $MgSiO_3$.[40] Nguyen *et al*. reported a mechanochemical synthesis of $MgCoSiO_4$, which produced average particle sizes of 27 nm but included 3% tungsten carbide milling impurities.[41]

The aim of this work was to develop a synthesis procedure for nanosized Ni- and Co-doped forsterites suitable for future *in situ* experimental studies on divalent metal silicate carbonation and concurrent Ni and Co recovery. Our targeted stoichiometries were $(Mg_{0.95}Ni_{0.5})_2SiO_4$, $(Mg_{0.75}Ni_{0.25})_2SiO_4$, $(Mg_{0.95}Co_{0.05})_2SiO_4$, and $(Mg_{0.75}Co_{0.25})_2SiO_4$; referred to as "5% NiFo," "25%NiFo," "5%CoFo," and "25%CoFo," respectively. Although these stoichiometries exceed natural Ni and Co levels in mafic and ultramafic rocks,[7,8] they are ideal for investigating how these metals influence forsterite carbonation rates and tracking their fate during the reaction. We verified size and purity using X-ray diffraction (XRD), surface area measurements, total carbon (TC) analysis, ultraviolet-visible (UV-Vis) spectroscopy, infrared (IR) spectroscopy, X-ray photoelectron spectroscopy (XPS), scanning electron microscopy (SEM), and transmission electron microscopy (TEM). Our synthesis method supports up to 25% metal doping, leads to nanoparticles as small as 29 nm, and avoids the formation of secondary phases.

2. Synthesis and characterization methods

2.1. Materials and standardizations

Cobalt(II) chloride (anhydrous, 99.7% metals basis) was purchased from Thermo Scientific. Nickel nitrate hexahydrate (99.999% metals basis), tetraethylorthosilicate (TEOS, ≥99.0%), dodecylamine (98%), and diphenylamine (≥99%) were purchased from Sigma-Aldrich. *tert*-Butylamine (99%) was purchased from Acros Organics. Magnesium methoxide (7%–8% in methanol), methanol (anhydrous, 99.9%), and toluene (anhydrous, 99.8%) were purchased from Alfa Aesar. Reagent water was de-ionized (Barnstead NanoPure) and had a resistivity of 18.2 MΩ cm. The magnesium content of the magnesium methoxide solution was analyzed in triplicate by drying approximately 5 grams of solution in a platinum crucible in air overnight and then firing the solid that remained at 1000 °C for 4 h to produce MgO powder. The molal concentration of magnesium was precisely determined based on the masses of solution and MgO and was typically 1.1 molal. Similarly, the Ni content of the nickel nitrate hexahydrate was determined in triplicate by massing approximately 0.7 grams into a platinum crucible and then firing at 1000 °C for 4 h to produce NiO powder. The amount of Ni per gram was calculated from the masses of nickel nitrate hexahydrate and NiO and was typically 0.00345 mol g^{-1}. All other reagents were assumed pure.

2.2. Synthesis method

The syntheses of pure and metal-doped forsterites each involved 3 steps: (1) reflux to make a sol-gel, (2) wash to remove excess surfactant from the gel, followed by drying of the gel to make a precursor powder to calcination, and (3) calcination of the precursor to make the target forsterite product.

The reflux step was carried out in a nitrogen glove box and used a 2 L, two-neck round-bottom flask topped with a condenser thermostated at 18 °C, an electric heating mantle, and a stir bar and stir plate. The volumes used of toluene and methanol solvents are given in Table 1 and the masses used of the reactants and reagents are summarized in Table 2. First, vials were prepared that contained the dodecylamine and *tert*-butylamine dissolved in toluene, diphenylamine dissolved in toluene (for Ni-doped forsterite syntheses), and either nickel nitrate hexahydrate or cobalt chloride dissolved in methanol (for Ni- or Co-doped syntheses, respectively). Second, initial volumes of toluene and methanol were added to the round-bottom flask with stirring. Third, magnesium methoxide in methanol solution was massed in a beaker and then quantitatively transferred to the round-bottom flask using the methanol wash. Fourth, TEOS was massed in a vial and then quantitat-

Table 1 Volumes of solvents used when carrying out refluxing step of undoped and metal-doped forsterite syntheses

	Volumes of toluene (mL)					Volumes of methanol (mL)			
Sample	Initial in flask	Wash	Dodecyl- and *tert*-butyl-amine	Diphenylamine	Total	Initial in flask	Wash	Ni or Co[a]	Total
Undoped	300	100	25	0	425	75	100	0	175
5%NiFo	275	100	25	25	425	0	150	25	175
25%NiFo	275	100	25	25	425	0	150	25	175
5%CoFo	300	100	25	0	425	0	150	25	175
25%CoFo	300	100	25	0	425	0	150	25	175

[a] Ni = nickel nitrate hexahydrate; Co = cobalt chloride.

Table 2 Amounts of reactants and reagents used when carrying out refluxing step of undoped and metal-doped forsterite syntheses[a]

								Water additions (mL)		
Sample	Magnesium methoxide (g)	TEOS (g)	Nickel nitrate hexa-hydrate (g)	Cobalt chloride (g)	Diphenyl-amine (g)	Dodecyl-amine (g)	*tert*-Butyl-amine (g)	1st	2nd	3rd
Undoped	65.401	7.404	0.000	0.000	0.000	8.750	1.750	2.0	2.0	2.0
5%NiFo	62.131	7.404	1.031	0.000	1.323	11.375	1.750	1.6	2.0	2.0
25%NiFo	49.051	7.404	5.156	0.000	6.616	8.750	1.750	0.0	2.0	2.0
5%CoFo	62.131	7.404	0.000	0.461	0.000	17.500	1.750	2.0	2.0	2.0
25%CoFo	49.051	7.404	0.000	2.307	0.000	8.750	1.750	2.0	2.0	2.0

[a] Both the magnesium methoxide in methanol solution and the nickel nitrate hexahydrate solid was standardized. The calculations for this table were based on standardizations that determined 1.0864 molal Mg content in the magnesium methoxide in methanol solution and 0.003447 moles Ni per gram of the nickel nitrate hexahydrate solid.

ively transferred to the round bottom flask, also using the methanol wash. For Ni-doped forsterite syntheses, the prepared bottle of diphenylamine in toluene was quantitatively transferred next to the round-bottom flask using some of the toluene wash. For Ni- or Co-doped forsterite syntheses, the prepared bottles of nickel nitrate hexahydrate or cobalt chloride dissolved in methanol were next quantitatively transferred to the round-bottom flask using the remaining methanol wash. Last, the prepared bottle of dodecylamine, *tert*-butylamine, and toluene mixture was quantitatively transferred to the round-bottom flask using remaining toluene wash. The heating mantle was turned to 160 °C to start a 24 h reflux where about 3 drops of solvent condensed and fell back into the solution per second. A first dropwise water addition was made 1 h after refluxing began; a second water addition was made about 6–8 h later; and the last water addition was made 2 h before the end of the refluxing step. Pictures of the reflux after water additions are shown in Fig. S1.† After 24 h, the heating mantle was turned off, and the solution was allowed to cool for an hour before capping the round-bottom flask and removing it from the glove box and transferring it to a fume hood.

The wash and drying steps were carried out in the fume hood. About a third of the solution was poured from the round-bottom flask into six 50 mL polytetrafluoroethylene centrifuge tubes that were spun at 2325 relative centrifugal force for 10 min. The solvent was discarded, and a gel was left in the bottom of the centrifuge tubes. The gel was washed three times by adding 10 mL of a 2 : 1 v/v mixture of toluene and methanol, resuspending the gel using a Vortex mixer, centrifuging for 10 min, and then discarding the solvent. After the third wash, the gel was suspended again in about 5 mL of the toluene–methanol solvent to transfer to a beaker. A gentle stream of N_2(g) was flowed over the gel overnight to evaporate the solvent, and exposure to CO_2 from the air was minimized. Pictures of the dried gel are shown in Fig. S2.† The dried gel was ground in an agate mortar and pestle to make a precursor powder to calcination.

The calcination of the precursor step was carried out in a 2500 cm^3 volume muffle furnace (Lindberg/Blue M box furnace, Thermo Scientific) that was purged with air at a flow of 800 mL min^{-1} for undoped and both 5% and 25% Co-doped forsterite. Calcination of the precursors for 5% and 25% Ni-doped forsterite was carried out in a 6250 cm^3 volume muffle furnace (Lindberg/Blue M box furnace, Thermo Scientific) that was purged with air at a flow of 2000 mL min^{-1}. A mass of 0.5 g of precursor power was placed in a platinum crucible. The precursor powders for each of the undoped and metal-doped forsterites were calcined according to the ramp time, soak time, and temperature conditions listed in Table 3 to make the target crystalline products.

2.3. Characterization methods

Powder X-ray diffraction patterns of pure and metal-doped forsterites were collected from powders packed into zero-background well holders using a Rigaku SmartLab SE diffractometer. The instrument employed Bragg–Brentano geometry with a Cu X-ray source (λ = 1.5418 Å), a variable divergence slit,

Table 3 Conditions used for the calcination step of undoped and metal-doped forsterite syntheses

Sample	Ramp time (min)	Soak time (min)	Calcination temperature (°C)
Undoped	10	120	775
5%NiFo	240	60	1100
25%NiFo	240	60	950
5%CoFo	10	120	975
25%CoFo	10	120	900

and a high-speed D/teX Ultra 250 1D detector. Patterns were collected between 2 and 100° 2θ at intervals of 0.01° 2θ. Rietveld analysis using TOPAS (v6, Bruker AXS) was carried using the forsterite structure published by Hushur *et al.*[42] with peak profiles modeled using the fundamental parameters approach implemented in TOPAS. Small amounts of metal oxide were identified through residual intensity near 42.5° 2θ and quantified in the Rietveld fit. Atomic coordinates and displacement parameters were fixed to their published values, and the Co or Ni occupancies of the M1 and M2 sites were refined in the doped samples. The crystallite sizes were determined from peak broadening using the double-Voigt convolutions in TOPAS, with the instrumental contribution modeled by the fundamental parameters and validated against a Si disc standard. The variation in peak breadth with 2θ indicated broadening by both limited size and microstrain and so both phenomena were modeled using Lorentz and Gauss broadening, respectively.

Pure and metal-doped forsterites were analyzed by the Brunauer Emmett Teller (BET) method[43] for specific surface area using a TriStar II Plus Surface Area and Porosity Analyzer from Micromeritics. Nitrogen gas adsorption and desorption isotherms were recorded at 77 K by means of volumetric adsorption in a relative pressure range, P/P_0, of 0.05–0.30. Specific surface area was calculated from these pressure ranges using the BET equation. Samples were prepared prior to analysis by degassing 0.75 g of material in vacuum (100 μmHg) at 50 °C overnight to remove humidity and possible contaminants.

The pure and metal-doped forsterites were analyzed for total carbon (TC) on a VarioEL Cube Elemental Analyzer (Elementar Analysensysteme GmbH, Langenselbold Germany) equipped with a thermal conductivity detector. Samples were weighed using a microbalance into tin foil boats and encapsulated. Combustion was at 1150 °C with an oxygen dose rate of 37 mL min^{-1} for 120 s.

Ultraviolet–visible (UV-Vis) hemispherical reflectance spectra of pure and metal-doped forsterites were collected with a UV-Vis spectrometer (Cary 5000) equipped with an integrating sphere (DRA-2500). The total reflectance from the samples, including both specular and diffuse components, was collected. Spectra were collected over the 300–900 nm range with 2 nm resolution and 0.5 nm data interval. Powders were loaded into a sample holder with a quartz window. The sample holder was placed on the sample port of the integrating sphere, with a Spectralon 99% diffuse reflectance plate on the reference port. Sample spectra were divided by the spectrum of a 99% diffuse reflectance standard (LabSphere, SRS-99-020).

Attenuated total reflection (ATR) IR spectra of pure and metal-doped forsterites were collected with a vacuum IR spectrometer (Bruker Vertex 80v) equipped with a single-bounce diamond ATR accessory (DiaMaxATR, Harrick Scientific). The diamond internal reflection element was covered with solid forsterite nanoparticles, and the anvil of the cell was used to press the solid onto the diamond. Spectra were collected at 4 cm^{-1} resolution and averaged over 512 scans. Mid-IR spectra were taken using a KBr beamsplitter and a DLaTGS detector, and far-IR spectra were taken using a multilayer Mylar beamsplitter and a DTGS detector with a polyethylene window.

X-ray photoelectron spectroscopy (XPS) measurements were performed using a Thermo Fisher NEXSA spectrometer with a 125 mm mean radius, full 180° hemispherical analyzer, and 128-channel detector. This system uses a focused monochromatic Al K_α X-ray (1486.7 eV) source for excitation at a power of 150 W and an electron emission angle of 60°. The vacuum chamber pressure was ~2.7 × 10^{-7} Pa during the measurements. Survey scans were collected using an analyzer pass energy of 140 eV and a step size of 0.5 eV. Regional (high-resolution) scan spectra were collected using a pass energy of 50 eV with a step size of 0.1 eV. For the Ag $3d_{5/2}$ line, these conditions produced a full width at half maximum of 0.84 ± 0.02 eV. The instrument work function was calibrated to give a binding energy (BE) of 83.96 ± 0.05 eV for the Au $4f_{7/2}$ photoelectron line for clean metallic gold, and the spectrometer dispersion was adjusted to give a BE of 932.62 ± 0.05 eV for the Cu $2p_{3/2}$ line of clean metallic copper. A charge neutralization system was used for all analyses using a magnetic immersion lens and electron charge neutralization with the electron neutralizer controlled at 1.0 eV bias voltage, 1.95 A filament current, and 3.7 eV charge balance. High-resolution scans were collected for the Mg 2s, Si 2p, C 1s, O 1s, Co 2p, and Ni 2p photoelectron lines. Two high-resolution scans at spatially separated spots were collected for each sample. Absolute peak positions were determined by charge correcting to the adventitious (C–C/C–H) C 1s line at 285.0 eV.

Scanning electron microscopy (SEM; Thermo Fisher Scientific Helios NanoLabTM 600i) was used to image the particle morphologies of the undoped and metal-doped forsterites. Powders were suspended in isopropanol (5 g L^{-1} solid concentration) and dispersed by sonication. A volume of 0.1 mL of this suspension was added to a 1 cm^2 glass slide, and the isopropanol was evaporated under nitrogen gas flow. The powders fixed to the slide were coated with a 10 nm thick C layer to reduce sample charging during imaging.

High-resolution transmission electron microscopy (TEM) of undoped and metal-doped forsterites was performed using an aberration corrected Thermo-Fisher Themis Z scanning/transmission electron microscope with a high-angle annular dark

field (HAADF) detector. The probe convergence angle was 25 mrad, and the inner detection angle on the HAADF detector was 52 mrad. All images were collected using multi-frame integration, mostly consisting of 20–40 images. Energy dispersive X-ray (EDX) analysis was performed in multi-frame acquisition mode using a Thermo-Fisher Super-X silicon drift detector. The system achieves ~0.8 steradian solid collection angle. The microscope was operated at 300 kV, and during the elemental mapping, the probe current was around 75 pA. In the EDX elemental mapping, a series of 512 × 512 pixel size images were captured with 20 μs dwell time. The acquisition and image processing were performed with Thermo-Fisher's Velox software.

3. Results and discussion

We synthesized undoped, 5% Ni-doped, 25% Ni-doped, 5% Co-doped, and 25% Co-doped forsterites suitable for *in situ* experimental studies with crystallite sizes less than 100 nm, less than 1 wt% oxide, and specific surface area greater than 10 m^2 g^{-1}. For undoped forsterite, we adapted the reverse microemulsion sol–gel method reported by Anovitz *et al.*[35] for nanosized forsterite. Reactants magnesium methoxide and TEOS were refluxed in a 2 : 1 (v/v) toluene : methanol solvent containing dodecylamine as the surfactant, tertbutylamine as the hydrolysis agent, and a small stoichiometric excess of water. This reflux step produced a precursor gel that is likely mostly amorphous silica and magnesium (hydr)oxide with some Si–O–Mg linkages encapsulated in micelles of dodecylamine. The gel was washed to remove excess dodecylamine, dried to remove solvent, and ground. Finally, the dried precursor was calcined to burn the dodecylamine and produce a crystalline forsterite product.

For the Ni- and Co-doped forsterites, a stochiometric amount of magnesium methoxide was replaced with a reactant containing the target metal. Nickel and cobalt alkoxides could not be used as reactants because they are polymeric and insoluble.[44–46] Instead, the reactant we used for Co-doped forsterites that led to successful nanosized material was anhydrous cobalt chloride. For Ni-doped forsterites, syntheses using anhydrous nickel chloride failed to produce a product without a significant MO impurity (M = Ni and/or Mg). The reactant that led to successful nanosized material was nickel nitrate hexahydrate. We added diphenylamine as a sacrificial reductant to avoid oxidation of the dodecylamine surfactant by nitrate during Ni-doped forsterite syntheses. Diphenylamine (or its reaction product with nitrate) may additionally participate in the microemulsion as a co-surfactant. Although Anovitz *et al.* emphasized the importance of initially preparing the microemulsion without any water,[35] we did not find the water in nickel nitrate hexahydrate to negatively affect the Ni-doped forsterite syntheses. However, the initial water additions for our Ni-doped forsterite syntheses were reduced accordingly (Table 2).

A key parameter controlling the size and porosity of the precursor particles was the dodecylamine concentration (see Table 2). Specifically, it is important that the dodecylamine is above the critical micelle concentration during the reflux step. Substitution of magnesium methoxide with cobalt chloride or nickel nitrate hexahydrate may further change the surfactant properties of dodecylamine and the micelle sizes. Specific ion effects suggest that chloride and nitrate anions would affect micellar properties differently.[47–49] Because the reactants of each metal-doped forsterite synthesis have different micellar interactions, the successful concentrations of dodecylamine surfactant were determined iteratively (Table 2). The porosity of the precursor gels was also observed to affect the combustion of the leftover organics, mainly dodecylamine, in the precursor. If the precursor is not sufficiently porous, then oxygen cannot penetrate the particles to burn the dodecylamine before it pyrolyzes to form a temperature resilient soot. Another possible reason we believe that calcination does not completely burn the dodecylamine is related to how the solvent was dried from the precursor gel after the washing step. If the gel is dried in air, then the metal (hydr)oxides will react with CO_2 to form metal carbonates, which are often used as catalysts for the pyrolysis of biomass.[50–52] Drying under nitrogen preserves Mg, Ni, and/or Co as (hydr)oxides so that dodecylamine can be preferentially oxidized instead of pyrolyzed.

Finding the best calcination conditions (see Table 3) was also an iterative process. Generally, both Co- and Ni-doped forsterites required higher calcination temperatures than the undoped forsterite to avoid metal oxide contaminants, such as Co_3O_4 and MO (M = Mg and/or Ni). Higher temperatures often led to larger crystallite sizes by XRD analysis and lower specific surface areas than for undoped forsterite. Faster ramp rates were important for minimizing metal oxide contamination in the Co-doped forsterites. We speculate that this is because Co-containing metal oxides likely grow faster than the Co-doped forsterite at lower temperatures, but forsterite is more stable and grows faster than the metal oxides at higher temperatures. Interestingly, using fast ramp rates for the Ni-doped forsterites led to particles with small crystallite sizes, but the particles were so badly sintered that the specific surface areas were less than 1 m^2 g^{-1}. Hence, the Ni-doped forsterites required slower ramp rates and higher calcination temperatures to avoid metal oxide contamination.

3.1. X-ray diffraction

Powder X-ray diffraction was used to determine the mineralogical composition of the samples and to determine the extent of the coherent forsterite lattice (*i.e.* crystallite size). The physical particles may be larger, but not smaller, than the crystallite size indicated by powder XRD. The powder XRD patterns and Rietveld refinement residuals of undoped and Ni- and Co-doped forsterite products are shown in Fig. 1, and the results of Rietveld refinements of these patterns are in Table 4. Good agreement between calculated and measured patterns was obtained, based on low residuals and weighted profile *R*-factors (R_{wp}). Only small quantities of metal oxide were detected in the undoped forsterite (0.6 wt%) (Fig. S3†) and the 25% Ni-doped forsterite (0.4 wt%). The estimated crystallite sizes for the forsterites (Table 4) ranged from 29 nm for the 25% Ni-doped sample to 83 nm for 5% Ni-

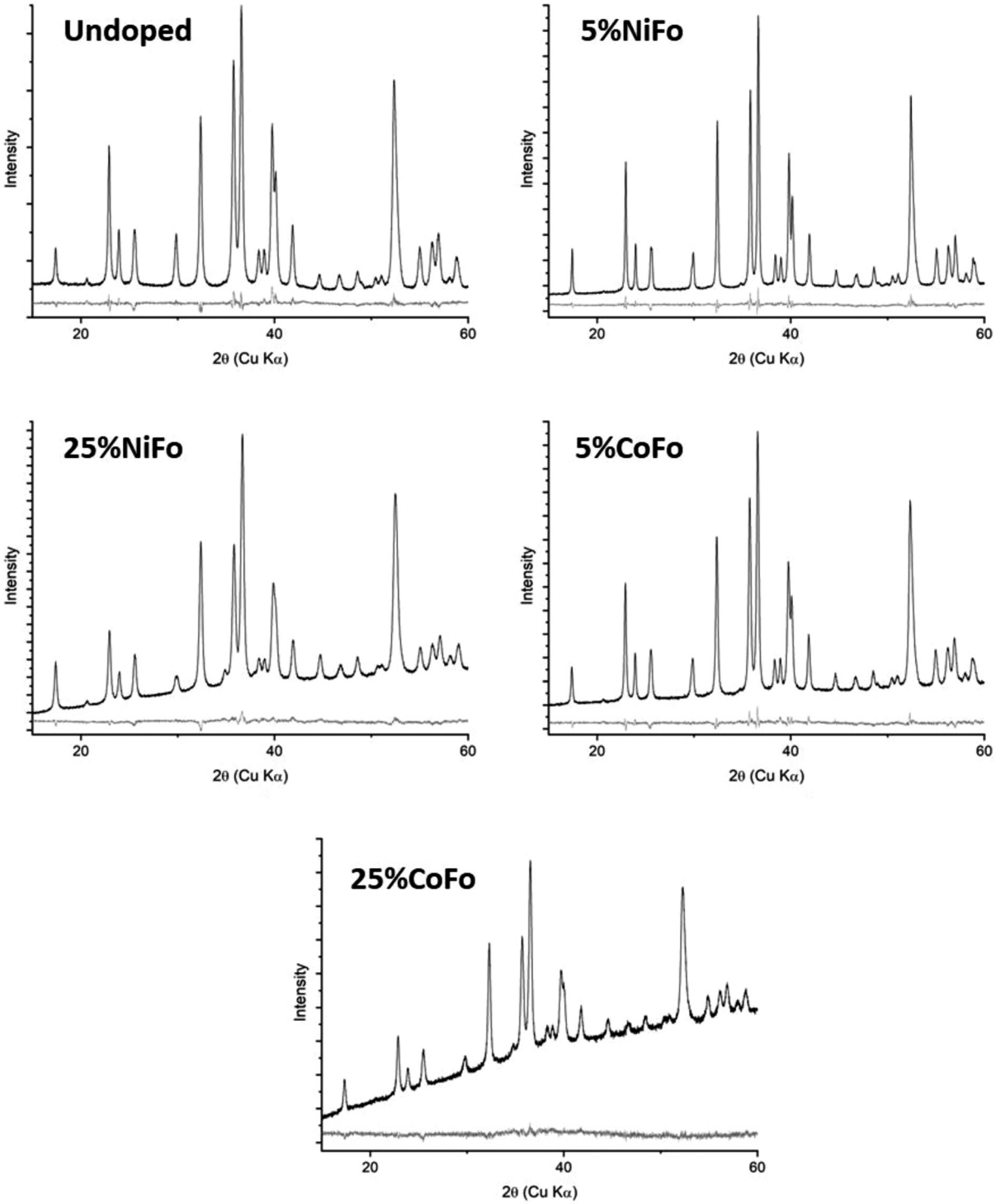

Fig. 1 XRD patterns of undoped and Ni- and Co-doped forsterites (black traces). Residuals from Rietveld refinements are shown below each pattern (gray traces). 5%NiFo, 5%CoFo, and 25%CoFo required only a one component fit, but undoped forsterite and 25%NiFo required an additional component due to an MO impurity, where M = Mg or Mg and Ni, respectively.

doped forsterite. Lattice parameters and unit cell volumes (Table 4) increased with increasing percent Co, which is consistent with the replacement of smaller Mg^{2+} with larger Co^{2+}. The opposite was true for the Ni-doped samples, where lattice parameters and unit cell volumes decreased with increasing percent Ni, consistent with replacement of larger Mg^{2+} with smaller Ni^{2+}. The trends in the lattice parameters and cell volumes with percent metal substitution were not linear, but these trends resemble those reported in previous studies of Ni- and Co-doped forsterites.[53] Both Co and Ni show a strong preference for M1

Table 4 Results of Rietveld refinements of XRD patterns, specific surface areas, and total carbon analysis results of undoped and metal doped forsterites

	Undoped	5%NiFo	25%NiFo	5%CoFo	25%CoFo
Results of Rietveld refinements of XRD patterns					
Forsterite wt frac. (wt%)	99.4(1)%	100%	99.6(1)%	100%	100%
a (Å)	4.747(1)	4.743(1)	4.743(1)	4.750(1)	4.759(1)
b (Å)	10.194(1)	10.191(1)	10.191(1)	10.206(1)	10.219(1)
c (Å)	5.977(1)	5.970(1)	5.956(1)	5.979(1)	5.981(1)
Volume (Å^3)	289.265(6)	288.575(4)	287.879(8)	289.824(6)	290.85(1)
Crystallite size (nm)	38.0(2)	82.7(5)	28.7(1)	50.5(3)	30.6(3)
Strain	0.00071(1)	0.000320(5)	0.00073(1)	0.00053(1)	0.00046(2)
X_M^{M1}, occupancy M1 (4a)	—	0.067(1)	0.368(1)	0.052(1)	0.316(3)
X_M^{M2}, occupancy M2 (4c)	—	0.000(1)	0.065(1)	0.004(1)	0.095(2)
K_D	—	72(100)	8.4(2)	14(5)	4.4(1)
Measured M content (%)	—	3.4(2)%	21.7(2)%	2.8(2)%	20.6(4)%
MO wt. frac. (wt%)	0.6(1)%	—	0.4(1)%	—	—
R_{wp}	3.91%	2.75%	1.15%	1.99%	1.16%
BET surface areas (m^2 g^{-1})	32(1)	14(1)	34(1)	11(1)	20(1)
Total carbon analysis results (wt%)	0.13(3)	0.07(3)	0.04(3)	0.14(3)	0.09(3)

(tetragonally elongated octahedra) *versus* M2 (trigonally elongated octahedra) cation sites of the forsterite crystal structure.[53–57] The distribution constant K_D for the doped metal replacing Mg in the M1 site is $K_D = (X_M^{M1}(1 - X_M^{M2}))/(X_M^{M2}(1 - X_M^{M1}))$, where X_M^{M1} and X_M^{M2} are the M1 and M2 site occupancies, respectively, and M = Ni or Co. Consistent with previous studies,[53,55–58] K_D values (Table 4) were larger for Ni than for Co. The overall refined Co and Ni contents are the average of the M1 and M2 site occupancies and are slightly lower than the expected values.

3.2. Specific surface area and total carbon

BET specific surface areas are in Table 4 and were better than 30 m^2 g^{-1} for the undoped and 25% Ni-doped forsterites, while the 25% Co-doped forsterite was 20 ± 1 m^2 g^{-1}. The specific surface areas of the 5% Ni- and Co-doped forsterites were 14 ± 1 and 11 ± 1 m^2 g^{-1}, respectively. The higher calcination temperatures needed to prevent oxide formation in the 5%NiFo and 5%CoFo likely promoted crystallite growth and aggregation, leading to lower specific surface areas compared to their 25% doped counterparts. The specific surface areas only roughly correlated with the crystallite sizes from the XRD Rietveld refinement, and the deviations are likely due to particle aggregation. Despite some aggregation of particles, the specific surface areas of all four doped forsterites were higher than the targeted 10 m^2 g^{-1}. Total carbon (Table 4) was measured to check for soot contamination from unburnt dodecylamine during the synthesis calcination step and ranged from 0.04 ± 0.03 to 0.14 ± 0.03 wt%.

3.3. UV-Vis reflectance spectroscopy

To determine phase purity and to measure the electronic structure of the dopant cations, we measured the UV-Vis hemispherical reflectance spectra of the forsterites. The reflectance spectra were plotted as $\log_{10}(1/R)$ in Fig. 2, where absorbance bands are upward-going. Although quantitative information can be extracted from UV-Vis absorbance spectra directly, this is not true for diffuse reflectance spectra, which include both absorbance and scattering of light. Particle and aggregate sizes on the order of UV-Vis wavelengths will scatter light, increasing the path length and causing apparent deviations from the Beer–Lambert Law.[59] In the UV-Vis spectra of the Co-doped forsterite, the overall shape of the absorbance bands resembles that of previously published spectra of $(Co_{0.64}Mg_{0.36})_2SiO_4$.[60] The ten electronic transitions in this spectral region have been previously assigned in polarized absorption spectra of olivine single crystals.[60] While the ten transitions could not be fully resolved from a diffuse reflectance measurement of isotropically oriented particles, overlapping sets of peaks and individual peaks that could be identified were labeled in Fig. 2. Peaks labeled *a*, *c*, *f*, and *i* have been assigned to electronic transitions of Co^{2+} in M1 sites, with *b*, *d*, *e*, *g*, *h*, and *j* assigned to those in M2 sites.[60] The overall shape of the 5%CoFo and 25% CoFo spectra is similar to that of $(Co_{0.64}Mg_{0.36})_2SiO_4$,[60] indicating that Co similarly partitions into M1 sites in these forsterites. The relative peak heights of *a* and *i* are higher in the 5% CoFo spectrum than in the 25%CoFo spectrum, consistent with the XRD-derived occupancies (Table 4) that indicate 5% CoFo has a greater K_D than 25%CoFo.

The spectra of the Ni-doped forsterites, shown in Fig. 2, are also in good agreement with previously published spectra of Ni-containing olivine crystals.[58] The seven electronic transitions of Ni^{2+} in this spectral region can be identified in the 25% Ni-doped forsterite spectrum and are labeled in Fig. 2 according to previous assignments.[58] In the 5% Ni-doped forsterite spectrum, the smaller peaks *c*, *d*, *e*, and *f* are more difficult to distinguish than in the 25% Ni-doped forsterite spectrum due to the lower Ni content of the 5% Ni-doped forsterite. Transitions *a*, *c*, and *e* have been assigned to Ni^{2+} atoms in M1 sites, while transitions *b*, *d*, *f*, and *g* have been assigned to Ni^{2+} atoms in M2 sites.[58] While these diffuse reflectance spectra could not be used for quantification of M1/M2 occupancy or K_D, the relative heights of the *a* and *b* transitions differ between the 5%NiFo and 25%NiFo spectra. The greater height of peak *b* in the 25%NiFo spectrum suggests

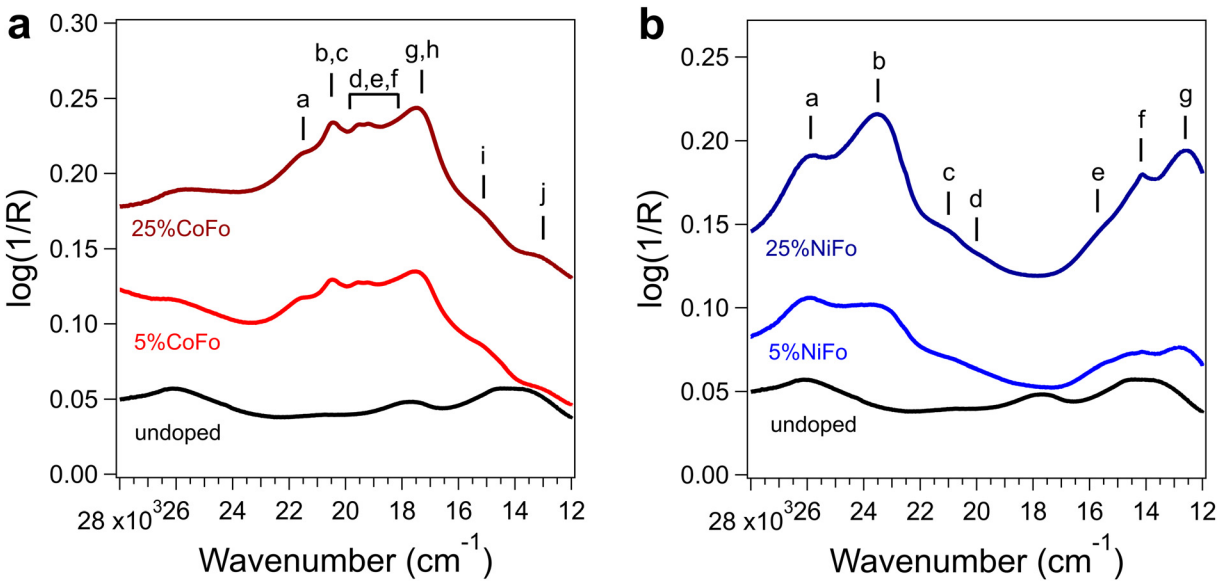

Fig. 2 (a) UV-Vis diffuse reflectance (R) spectra of undoped, 5% Co-doped, and 25% Co-doped forsterites. Groups of Co^{2+} absorbance bands labeled a–j according to assignments of Ullrich *et al.*[60] (b) UV-Vis diffuse reflectance spectra of undoped, 5% Ni-doped, and 25% Ni-doped forsterites. Ni^{2+} absorbance bands labeled a–g according to assignments of Hu *et al.*[58]

that its M1/M2 occupancy ratio is lower than that of 5%NiFo. While the XRD refinements (Table 4) did not find any Ni^{2+} occupying the M2 site in the 5%NiFo, the presence of peak b in the UV-Vis spectra suggests a small amount of Ni^{2+} atoms in M2 sites is below the detection limit of the XRD refinement. Peak b, the M2 $^3A_2 \rightarrow {}^3T_1$ transition, is the Ni^{2+} transition in Ni_2SiO_4 with the greatest average linear absorption coefficient of 805 cm^{-1},[58] so UV-Vis spectra are sensitive to small changes in M2 occupancy in this band. The Ni-doped forsterite spectra were also useful in identifying secondary phases that can form during forsterite precursor calcination. NiO has a strong absorbance band at 14 115 cm^{-1} with a linear absorption coefficient of 950 cm^{-1}.[61] Because this absorption coefficient is higher than that of all the averaged Ni^{2+} transitions in Ni_2SiO_4,[58] NiO impurities are especially apparent in UV-Vis spectra. When the impurity is the mixed oxide (Ni,Mg)O, the absorbance band is shifted to 14 700 cm^{-1}.[62] UV-Vis reflectance spectra were used to determine the optimal calcination conditions to minimize formation of (Ni,Mg)O in the 5%NiFo (Fig. S4†). After calcination at 1100 °C, UV-Vis absorbance in the 5%NiFo spectrum (Fig. 2) at 14 700 cm^{-1} was not distinguishable from Ni-doped forsterite absorbances e and f. This is consistent with the XRD refinements (Table 4), which did not detect MO (M = Mg and/or Ni) in 5%NiFo.

3.4. FTIR spectroscopy

The mid-IR and far-IR spectra of the forsterites are shown in Fig. 3. Infrared peaks of olivines have previously been assigned across the forsterite–fayalite series.[63,64] The mid-IR bands of the undoped and doped forsterites match those typically found in forsterite infrared spectra and are assigned to stretching and bending modes of SiO_4 tetrahedra.[63,64] Substitution of Mg in forsterite with heavier metal atoms generally causes IR bands to redshift. The bands that redshift in the doped forsterites include one of the symmetric stretching bands (ν_3), the asymmetric bending bands (ν_4) between 650–490 cm^{-1}, and one symmetric bending band (ν_2) at 471 cm^{-1}. The set of SiO_4 vibrational modes and their red shifts indicate that Ni and Co atoms are incorporated into the forsterite lattice, consistent with XRD measurements. Full tabulation of IR peaks can be found in Table S1.† In the far-IR absorbance spectrum of forsterite thin films, peaks from 388–270 cm^{-1} are assigned to metal translations, and small bands at 202 and 144 cm^{-1} are assigned to SiO_4 translations.[63] In the undoped forsterite spectrum in Fig. 3, small SiO_4 translation bands are indeed found at 201 and 142 cm^{-1}, while the overlapping metal bands from 385–260 cm^{-1} differ in shape from thin film spectra. As with mid-IR spectra, far-IR bands redshift with substitution of Mg for Ni or Co. The 354 cm^{-1} metal translation band red shifts up to 345 cm^{-1} in the 25%NiFo spectrum and up to 340 cm^{-1} in the 25%CoFo spectrum, consistent with incorporation of heavier metal atoms in the forsterite lattice. The 25% Ni- and Co-doped spectra also have a band at 304 cm^{-1} and 296 cm^{-1}, respectively, that is not apparent in the undoped or 5% doped spectra. This band is not observed in thin film absorbance spectra of Mg–Fe olivines with iron content up to $(Mg_{0.75}Fe_{0.25})_2SiO_4$,[63] suggesting that this feature correlates with the partitioning of Ni and Co into M1 sites.

3.5. X-ray photoelectron spectroscopy

XPS analysis of the synthesized nanoparticles first involved performing survey scans (Fig. S5†). Besides an expected and unavoidable small amount of adventitious carbon, the survey scans showed that the near-surface regions of the forsterites

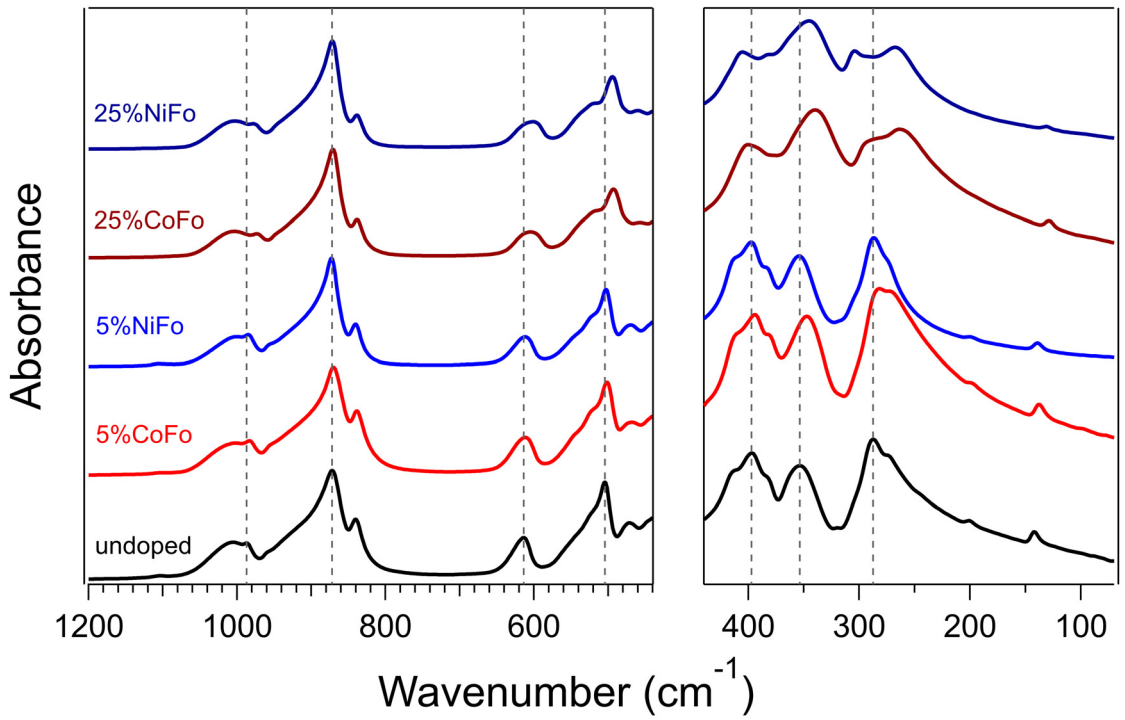

Fig. 3 ATR-FTIR spectra of synthetic forsterites in the 1200–440 cm^{-1} range (left) and the 440–80 cm^{-1} range: undoped forsterite (black trace), 5% and 25% Co-doped forsterite (red traces), and 5% and 25% Ni-doped forsterite (blue traces). Gray dashed lines mark peaks in the undoped forsterite spectrum. Spectra were normalized to the 871 cm^{-1} peak.

were free of detectable impurities. Regional scans of the Ni 2p photoelectron line (left panel of Fig. 4) showed a satellite structure typical of Ni(II) with a spin–orbit splitting energy (ΔNi 2p = BE(Ni $2p_{1/2}$) − BE(Ni $2p_{3/2}$)) of 17.5 eV, in good agreement with values obtained for NiO (17.4 eV),[65] $Ni(OH)_2$ (17.6 eV),[66] and olivine-supported Ni_2SiO_4 (17.7 eV).[67] Regional scans of

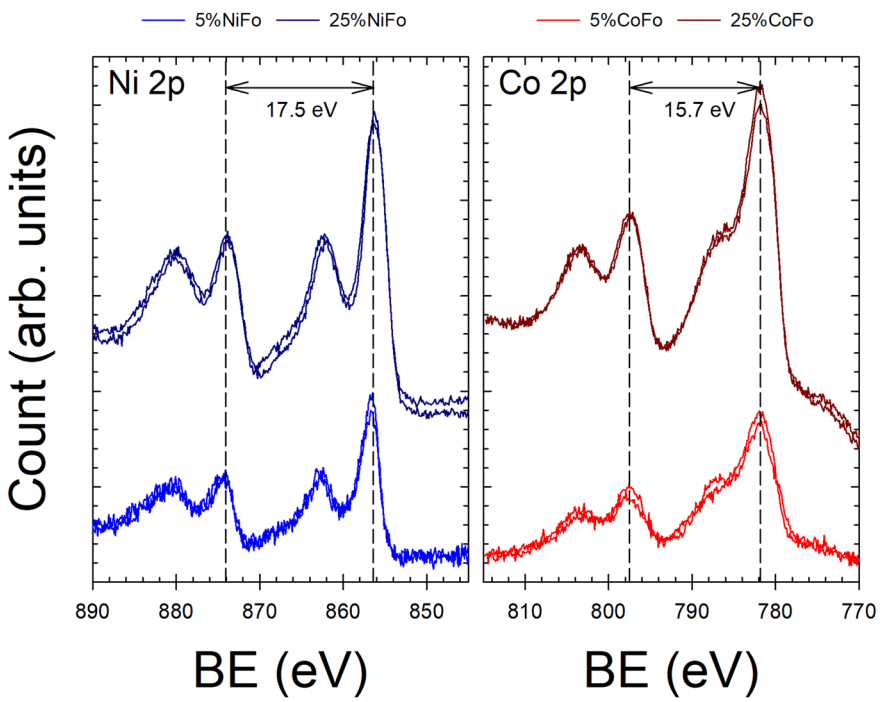

Fig. 4 Ni 2p and Co 2p XPS spectra (regional scans) of 5% and 25% Ni-doped (left, blue traces) and 5% and 25% Co-doped (right, red traces) forsterites. The spectra of two spatially separated spots are shown in each case.

the Co 2p photoelectron line (right panel of Fig. 4) also showed a satellite structure expected for Co(II). ΔCo 2p was 15.7 eV, within the range of values reported for Co_2SiO_4 by Ming and Baker (15.5 eV),[68] Guo and Wang (15.9 eV),[69] and Okamoto *et al.* (15.9 eV).[70] We conclude that Ni and Co were present as Ni(II) and Co(II), respectively, in the doped forsterites, which were thus free of potential oxidation products such as Co_3O_4. The Ni $2p_{3/2}$ BE was 856.4 eV, in good agreement with the value obtained by Zhao *et al.*[67] for olivine-supported Ni_2SiO_4 (856.6 eV once accounting for the difference in binding energies used for determining absolute peak positions). In NiO, the most likely Ni oxide contaminant, the Ni $2p_{3/2}$ BE is lower by several electron-volts (853.7 eV).[71] The Ni 2p regional scans in Fig. 4 showed no sign of a peak at this lower binding energy. The Ni $2p_{3/2}$ main peak position and the lack of any other main peaks indicated that Ni was only present as incorporated in forsterite in the Ni-doped forsterite samples. Similarly, the Co $2p_{3/2}$ BE (781.8 eV) was consistent with those reported by Ming and Baker (781.6 eV)[68] and Okamoto *et al.* (781.3 eV)[70] and distinct from the BEs of CoO (779.6–780.0 eV)[72–74] and Co_3O_4 (779.6–779.9 eV).[70,73] Here again, because the Co 2p regional scans (Fig. 4) did not show evidence of an additional main peak at lower binding energies, analysis of the XPS spectra indicated that Co was only present as incorporated in forsterite.

Analyses of high-resolution scans of the Mg 2s, Si 2p, O 1s, Ni 2p, and Co 2p photoelectron lines resulted in O/Si and Mg/Si atomic ratios for pure forsterite with average values of 4.2 and 1.6, respectively (Table 5). The O/Si atomic ratio agreed within uncertainties with that reported by Zakaznova-Herzog *et al.* (4.0 ± 0.8) for a vacuum-fractured natural Mg-rich olivine ($(Mg_{0.87}Fe_{0.13})_2SiO_4$),[75] whereas the Mg/Si atomic ratio was

Table 5 XPS analysis of undoped, 5% Ni-doped, 25% Ni-doped, 5% Co-doped, and 25% Co-doped forsterites. Atomic percents and ratios from high-resolution scans of Mg 2s, Si 2p, O 1s, Ni 2p, and Co 2p photoelectron lines. Results for two spatially separated spots ("Pos.") are tabulated

Sample	Pos.	Mg	Si	O	Ni	Co	O/Si	M/(M + Mg)	(M + Mg)/Si
Undoped	1	24.10	14.63	61.27	0.00	0.03	4.19	0	1.65
Undoped	2	23.73	14.82	61.39	0.00	0.00	4.14	0	1.60
5%NiFo	1	18.32	12.52	67.75	1.41	0.00	5.41	0.07	1.58
5%NiFo	2	18.13	12.34	68.12	1.41	0.00	5.52	0.07	1.58
25%NiFo	1	19.09	13.74	60.36	6.81	0.00	4.39	0.26	1.88
25%NiFo	2	19.19	13.72	60.51	6.57	0.00	4.41	0.26	1.88
5%CoFo	1	22.91	14.45	60.41	0.00	2.23	4.18	0.09	1.74
5%CoFo	2	22.99	14.45	60.29	0.00	2.26	4.17	0.09	1.75
25%CoFo	1	18.06	15.23	59.97	0.00	6.73	3.94	0.27	1.63
25%CoFo	2	18.15	15.25	59.66	0.00	6.94	3.91	0.28	1.64

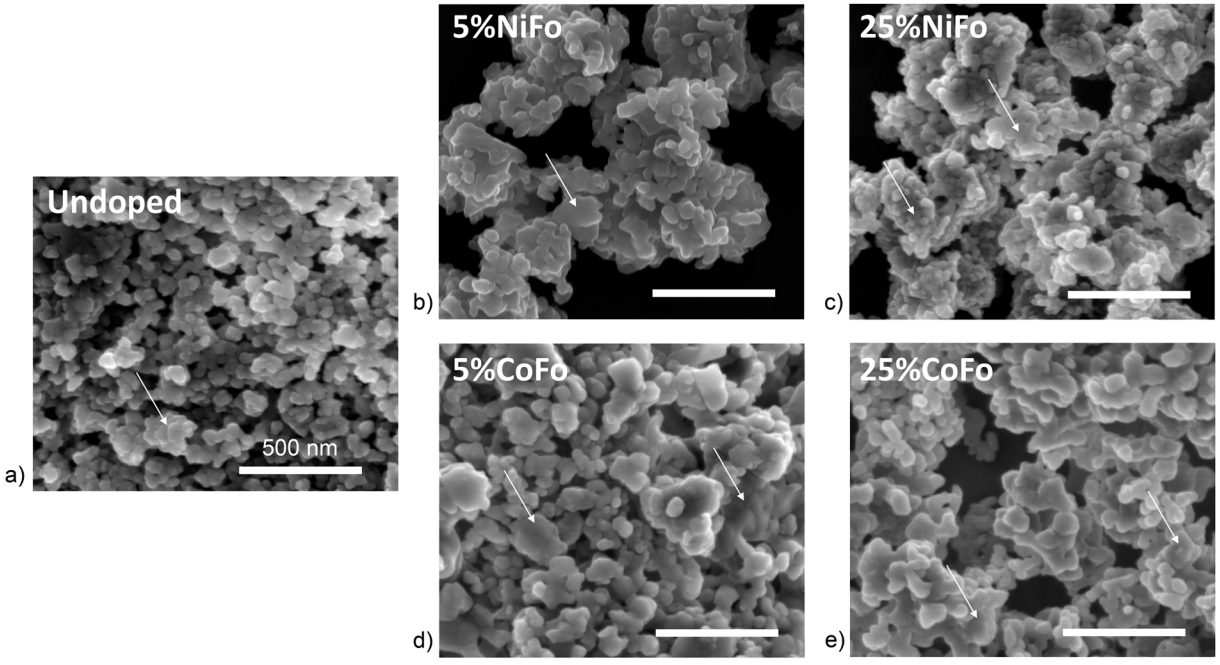

Fig. 5 SEM imaging of the (a) undoped forsterite, (b) 5% Ni-, (c) 25% Ni-, (d) 5% Co-, and (e) 25% Co-doped samples. White arrows highlight examples where particle fusion can be seen.

slightly lower than the (Mg + Fe)/Si ratio of Zakaznova-Herzog *et al.* (1.85 ± 0.9).[75] XPS analysis by Talik *et al.*[76] of a synthetic olivine with a lower Fe content ($(Mg_{0.94}Fe_{0.06})_2SiO_4$) than the natural sample analyzed by Zakaznova-Herzog *et al.*[75] yielded O/Si and (Mg + Fe)/Si ratios of 4.1 and 1.7, respectively. We conclude that the measured O/Si ratio was in line with expectation and that Mg might have been slightly depleted at the particle surfaces. The (Mg + Ni)/Si and (Mg + Co)/Si ratios of the doped forsterites fluctuated around the value obtained for pure forsterite with minimum and maximum values of 1.6 and

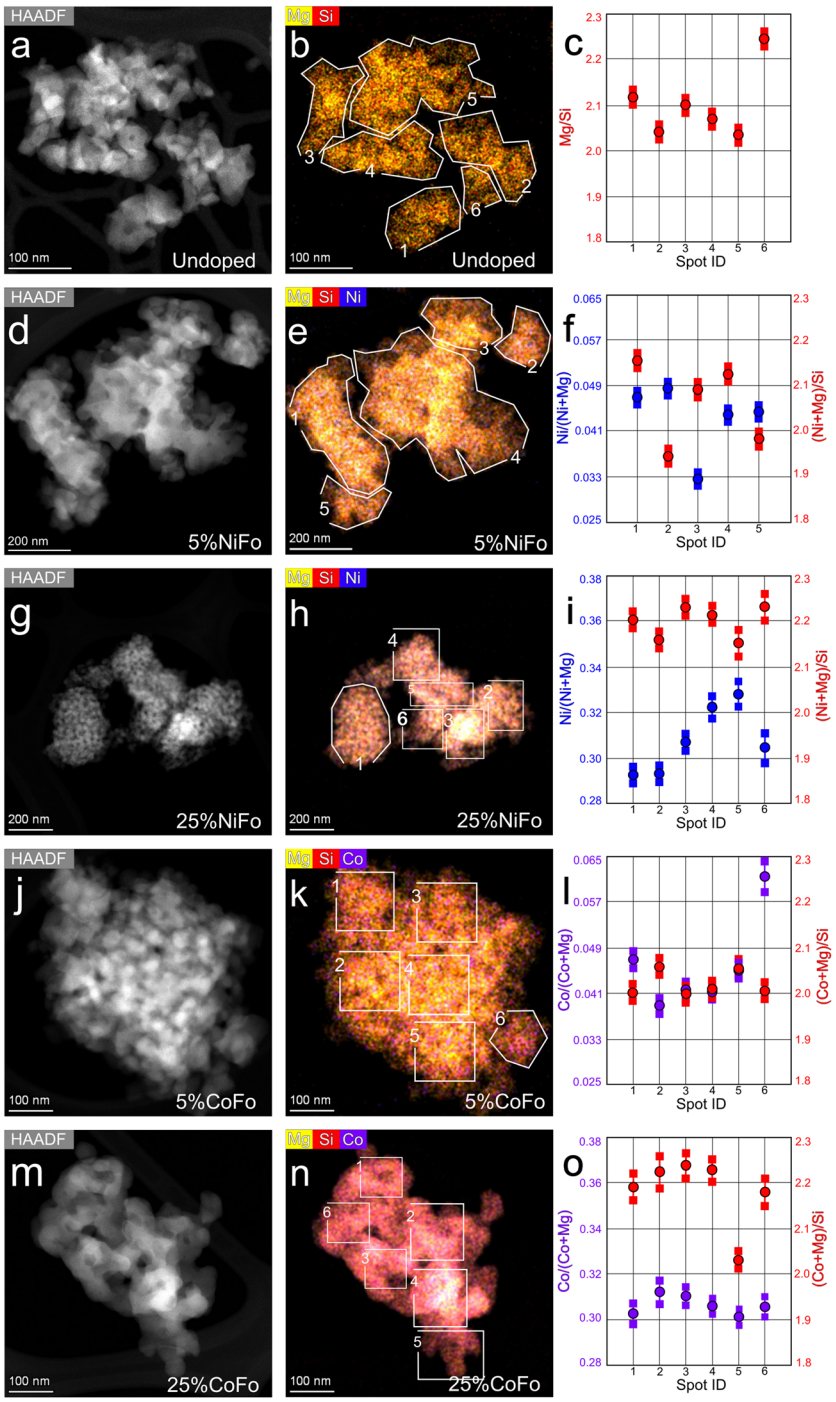

Fig. 6 The morphologies and chemical compositions of the undoped and Ni- or Co-doped forsterite particles according to STEM analyses. (a, d, g, j, and m) low magnification STEM HAADF images with (b, e, h, k, and n) the corresponding STEM EDX elemental maps. For the chemical characterization of the particles, we segmented the images into six regions and (c, f, i, l, and o) calculated the corresponding Ni/(Ni + Mg) or Co/(Co + Mg) and total metal/Si ratios from the EDX spectra.

1.9 (Table 5) for 5%NiFo and 25%NiFo, respectively, suggesting slight variations of the extent of cation depletion with the maximum value being consistent with the (Mg + Fe)/Si ratio of the vacuum-fractured olivine of Zakaznova-Herzog *et al.*[75] The Ni/(Mg + Ni) and Co/(Mg + Co) atomic ratios for the 25% doped forsterites were slightly higher than the nominal values but within uncertainties, assuming a quantification error between 5% and 10% on the atomic percents. The differences between measured and expected Ni/(Mg + Ni) and Co/(Mg + Co) ratios for the 5% doped forsterites were somewhat greater than expected based on quantification errors, suggesting either a slightly higher Ni/Co content than targeted or a small extent of Ni/Co surface segregation. These slightly high atomic ratios contrast with the XRD results, which found slightly lower Ni/Co content than targeted. The gel washing step of the synthesis is not expected to remove significant amounts of Mg or Ni/Co from the gel, and addition of too much Ni/Co to the synthesis would lead to significantly more oxide formation than found by XRD. These limits in the synthesis procedure suggest the exact amount of Ni/Co in the doped forsterites is close to the target amount and within the quantification errors of XRD and XPS.

3.6. Scanning electron microscopy

SEM imaging shows the general particulate morphology across the undoped and metal-doped forsterite samples (Fig. 5a–e). All the forsterite samples are nanoparticulate in nature (typically within the size range of ~30–90 nm) and irregular in shape. While all the samples are also highly aggregated, the nanoparticles in the doped samples appear to have a higher tendency to fuse together and form larger particles compared to that observed for the undoped forsterite. For instance, the undoped forsterite largely consists of individual nanoparticles within the size range of ~30–100 nm (Fig. 5a). In comparison, the 25% Ni-doped forsterite also consists of individual nanoparticles within the ~40–80 nm size range though larger particles and instances of particle fusion are also noticeable (Fig. 5c). These observations are similar to those for 5% Ni-doped (Fig. 5b) and Co-doped forsterites (Fig. 5d and e). The increased particle fusion in the doped forsterites was likely caused by the higher calcination temperatures (Table 3) needed to prevent the formation of secondary oxide phases in the doped forsterites.

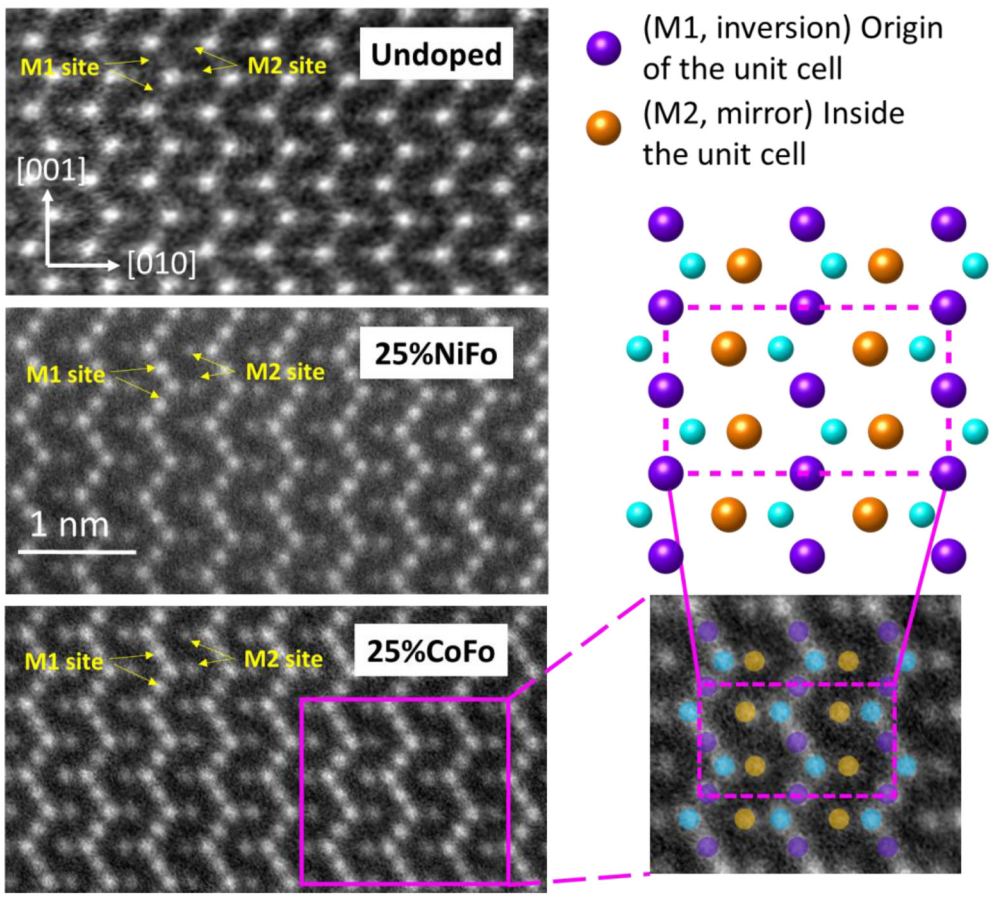

Fig. 7 HAADF atomic level observations from [1 0 0] resolving the M1 and M2 sites for undoped and 25% Ni- and 25% Co-doped forsterite. A comparison of the intensities of the M1 and M2 sites indicates Ni and Co prefer M1 sites.

3.7. Transmission electron microscopy and energy dispersive X-ray spectroscopy

Low magnification scanning transmission electron microscopy (STEM) micrographs showed particles with aggregate-like appearances (Fig. 6), similar to what was observed in the SEM analyses. To characterize the chemical composition and the elemental distribution of the particles, STEM EDX elemental mapping was performed on individual aggregates. We segmented the elemental maps of each aggregate into five or six zones, then extracted and evaluated quantitatively the corresponding EDX spectra. The metal ratios (Ni/(Ni + Mg) and Co/(Co + Mg)) and total-metal-to-silicon ((Ni + Mg)/Si or (Co + Mg)/Si) ratios for each area were calculated. The elemental maps suggested that the Ni and Co distributions within the particles were homogeneous while the calculated metal ratios showed minor inhomogeneities among the different regions of the aggregates.

In addition to the general morphological and structural analysis, atomic level HAADF observations were performed on the undoped, 25% Ni-doped, and 25% Co-doped forsterite to evaluate the distribution of Mg and Ni or Co among the available M1 and M2 sites. Ni or Co can be distinguished from Mg in HAADF observations due to their large differences in atomic numbers. It is expected that sites with higher proportion of Ni or Co will display much higher intensity due to the fact the contrast in atomic level HAADF images scales approximately as $Z^{1.7-1.9}$, where Z is the atomic number. Fig. 7 summarizes the atomic level observations performed on [100] in the Pbnm setting, which has proven to be particularly useful for independently resolving M1 (origin of the unit cell, inversion symmetry) and M2 (mirror plane) sites. For the 25% Ni- and Co-doped forsterite, the HAADF observations indicate greater intensity among M1 sites, suggesting preferential substitution of Ni and Co at these sites. The findings on M1 and M2 occupation from HAADF analysis are consistent with XRD and UV-Vis analyses and previous work.[54]

4. Conclusions

An anhydrous sol–gel surfactant protocol for synthesizing high-purity 5% and 25% Ni- and Co-doped forsterites has been developed. The method produces nm-sized crystallites, and while the calcination process causes some growth and fusion of particles, final products can be obtained with specific surface areas in the range 11–34 $m^2\ g^{-1}$. These values are comparable to those for pure nanosized forsterites used in previous carbonation studies,[16–18,23–25] and the specific surface areas are higher than the 10 $m^2\ g^{-1}$ needed to observe reactivity trends at laboratory time scales. XRD results showed minimal oxide formation of 0.6 wt% MgO in undoped forsterite and 0.4 wt% MO in 25%NiFo, while EDX metal ratios suggested some oxide presence in 25%NiFo and 25%CoFo.

The nanosized Ni- and Co-doped forsterites synthesized here will enable *in situ* experiments that address existing knowledge gaps regarding the mechanisms affecting metal silicate carbonation efficiency and the fate of Co and Ni. For example, while surface passivation is known to slow or halt the carbonation of mafic and ultramafic silicates in some reaction conditions, predictive models for this process are still lacking, and the influence of Ni and Co on the development of passivation layers is not yet understood. Furthermore, the thermodynamic and kinetic factors governing the partitioning of Ni and Co into secondary phases during carbonation-based extraction and separation processes remain unclear. A fundamental understanding of these processes will help the development of clean energy technologies that enhance the recovery of Ni and Co from mafic and ultramafic rocks.

For future synthesis of nanosized forsterites with other doping concentrations below 25%, this synthesis suggests some principles for the challenge of optimizing crystallite size and specific surface area while minimizing oxide formation. Higher calcination temperatures are needed for Ni- and Co-doped forsterites than undoped forsterite to prevent oxide formation. Introduction of different concentrations of anions or different anions alters the solvent-in-oil microemulsion, making surfactant concentration the key parameter to modify to produce a porous precursor at any dopant concentration. Further modifications to the procedure that could be evaluated are different nonionic surfactants, such as the Brij series, Igepal CO-520, or Triton X-100.

Author contributions

Kelly Peterson: Investigation, visualization, writing – original draft, writing – review & editing. Mark Bowden: Formal analysis, investigation, writing – original draft. Bavan Rajan: Investigation. Tenley Webb: Investigation. Bridgette Carven: Investigation. Libor Kovarik: Formal analysis, investigation, visualization. Zsombor Molnár: Formal analysis, visualization. Mark Engelhard: Investigation. Sandra Taylor: Investigation, visualization. Elsa Cordova: Investigation. Thomas Wietsma: Investigation. Sebastian Mergelsberg: Methodology, writing – review & editing. Christopher Thompson: Writing – review & editing. Sebastien Kerisit: Conceptualization, formal analysis, funding acquisition, project administration, writing – review & editing. John Loring: Conceptualization, funding acquisition, investigation, methodology, writing – original draft, writing – review & editing.

Data availability

Synthesis photographs, additional infrared spectroscopy data, and XPS survey scans are available in the ESI.†

Conflicts of interest

There are no conflicts to declare.

Acknowledgements

This work was supported by the U.S. Department of Energy, Office of Science, Office of Basic Energy Sciences, Chemical and Materials Sciences to Advance Clean Energy Technologies and Low-Carbon Manufacturing (FWP 80281). Pacific Northwest National Laboratory (PNNL) is operated for the DOE by Battelle Memorial Institute under contract DE-AC05-76RL01830. A portion of this research was performed on a project award (10.46936/lser.proj.2023.60770/60008927) from the Environmental Molecular Sciences Laboratory, a DOE Office of Science User Facility sponsored by the Biological and Environmental Research program under Contract No. DE-AC05-76RL01830. B. P. Rajan, T. E. Webb, and B. N. Carven were supported by the Science Undergraduate Laboratory Internships program (SULI) of the U.S. Department of Energy, Office of Science, Office of Workforce Development for Teachers and Scientists (WDTS). We thank L. M. Anovitz for synthesis advice, I. I. Leavy for help with analyses, T. J. Johnson for use of UV-Vis instrumentation, and Y-S Jun for helpful discussions.

References

1 T. E. Graedel and A. Miatto, U.S. Cobalt: A Cycle of Diverse and Important Uses, *Resour., Conserv. Recycl.*, 2022, **184**, 106441.
2 U.S. Geological Survey, *Mineral commodity summaries 2024*, U.S. Geological Survey, Reston, VA, 2024.
3 A. Väyrynen and J. Salminen, Lithium ion battery production, *J. Chem. Thermodyn.*, 2012, **46**, 80–85.
4 K. Turcheniuk, D. Bondarev, V. Singhal and G. Yushin, Ten Years Left to Redesign Li-Ion Batteries, *Nature*, 2018, **559**, 467–470.
5 J. D. Applegate, 2022 Final List of Critical Minerals, U.S. Geological Survey, Department of the Interior, *Fed. Regist.*, 2022, **87**, 10381–10382.
6 M. Grohol and C. Veeh, *European Commission, Study on the Critical Raw Materials for the EU 2023 - Final Report*, European Commission, Luxembourg, 2023.
7 Q. Dehaine, L. T. Tijsseling, H. J. Glass, T. Törmänen and A. R. Butcher, Geometallurgy of cobalt ores: A review, *Miner. Eng.*, 2021, **160**, 106656.
8 G. M. Mudd and S. M. Jowitt, A Detailed Assessment of Global Nickel Resource Trends and Endowments, *Econ. Geol.*, 2014, **109**, 1813–1841.
9 R. G. McDonald and B. I. Whittington, Atmospheric acid leaching of nickel laterites review Part I. Sulphuric acid technologies, *Hydrometallurgy*, 2008, **91**, 35–55.
10 J. F. Slack, B. E. Kimball and K. B. Shedd, *Cobalt*, U.S. Geological Survey, Reston, VA, 2017.
11 R. Santos, A. Van Audenaerde, Y. Chiang, R. Iacobescu, P. Knops and T. Van Gerven, Nickel Extraction from Olivine: Effect of Carbonation Pre-Treatment, *Metals*, 2015, **5**, 1620–1644.
12 F. Wang, D. Dreisinger, M. Jarvis, T. Hitchins and L. Trytten, CO_2 mineralization and concurrent utilization for nickel conversion from nickel silicates to nickel sulfides, *Chem. Eng. J.*, 2021, **406**, 126761.
13 F. Wang and D. Dreisinger, Carbon mineralization with concurrent critical metal recovery from olivine, *Proc. Natl. Acad. Sci. U. S. A.*, 2022, **119**, e2203937119.
14 F. Wang and D. Dreisinger, An integrated process of CO_2 mineralization and selective nickel and cobalt recovery from olivine and laterites, *Chem. Eng. J.*, 2023, **451**, 139002.
15 S. Katre, P. Ochonma, H. Asgar, A. M. Nair, R. K and G. Gadikota, Mechanistic insights into the co-recovery of nickel and iron via integrated carbon mineralization of serpentinized peridotite by harnessing organic ligands, *Phys. Chem. Chem. Phys.*, 2024, **26**, 9264–9283.
16 S. T. Mergelsberg, B. P. Rajan, B. A. Legg, L. Kovarik, S. D. Burton, G. M. Bowers, M. E. Bowden, O. Qafoku, C. J. Thompson, S. N. Kerisit, E. S. Ilton and J. S. Loring, Nanoscale Mg-Depleted Layers Slow Carbonation of Forsterite (Mg_2SiO_4) When Water Is Limited, *Environ. Sci. Technol. Lett.*, 2023, **10**, 98–104.
17 S. N. Kerisit, S. T. Mergelsberg, C. J. Thompson, S. K. White and J. S. Loring, Thin Water Films Enable Low-Temperature Magnesite Growth Under Conditions Relevant to Geologic Carbon Sequestration, *Environ. Sci. Technol.*, 2021, **55**, 12539–12548.
18 C. J. Thompson, S. T. Mergelsberg, B. P. Rajan, P. F. Martin, S. N. Kerisit and J. S. Loring, Nanoscale control over water-film thickness using temperature modulation: tuning mineral carbonation reactivity, *Environ. Sci.: Nano*, 2024, **11**, 1412–1416.
19 Q. R. S. Miller, C. J. Thompson, J. S. Loring, C. F. Windisch, M. E. Bowden, D. W. Hoyt, J. Z. Hu, B. W. Arey, K. M. Rosso and H. T. Schaef, Insights into silicate carbonation processes in water-bearing supercritical CO_2 fluids, *Int. J. Greenhouse Gas Control*, 2013, **15**, 104–118.
20 H. T. Schaef, B. P. McGrail, J. L. Loring, M. E. Bowden, B. W. Arey and K. M. Rosso, Forsterite [Mg_2SiO_4] Carbonation in Wet Supercritical CO_2: An in Situ High-Pressure X-ray Diffraction Study, *Environ. Sci. Technol.*, 2013, **47**, 174–181.
21 J. S. Loring, Q. R. Miller, C. J. Thompson and H. T. Schaef, in *Science of Carbon Storage in Deep Saline Formations: Process Coupling Across Time and Spatial Scales*, ed. A. Ilgen and P. Newell, Elsevier, 2018, p. 336.
22 J. S. Loring, C. J. Thompson, Z. Wang, A. G. Joly, D. S. Sklarew, H. T. Schaef, E. S. Ilton, K. M. Rosso and A. R. Felmy, In situ infrared spectroscopic study of forsterite carbonation in wet supercritical CO_2, *Environ. Sci. Technol.*, 2011, **45**, 6204–6210.
23 E. Placencia-Gómez, S. N. Kerisit, H. S. Mehta, O. Qafoku, C. J. Thompson, T. R. Graham, E. S. Ilton and J. S. Loring, Critical Water Coverage during Forsterite Carbonation in Thin Water Films: Activating Dissolution and Mass Transport, *Environ. Sci. Technol.*, 2020, **54**, 6888–6899.

24 C. E. Wood, O. Qafoku, J. S. Loring and A. M. Chaka, Role of Fe(II) Content in Olivine Carbonation in Wet Supercritical CO_2, *Environ. Sci. Technol. Lett.*, 2019, **6**, 592–599.
25 S. T. Mergelsberg, S. N. Kerisit, E. S. Ilton, O. Qafoku, C. J. Thompson and J. S. Loring, Low temperature and limited water activity reveal a pathway to magnesite *via* amorphous magnesium carbonate, *Chem. Commun.*, 2020, **56**, 12154–12157.
26 D. E. Giammar, R. G. Bruant Jr. and C. A. Peters, Forsterite dissolution and magnesite precipitation at conditions relevant for deep saline aquifer storage and sequestration of carbon dioxide, *Chem. Geol.*, 2005, **217**, 257–276.
27 E. H. Oelkers, J. Declercq, G. D. Saldi, S. R. Gislason and J. Schott, Olivine dissolution rates: A critical review, *Chem. Geol.*, 2018, **500**, 1–19.
28 G. D. Saldi, D. Daval, G. Morvan and K. G. Knauss, The role of Fe and redox conditions in olivine carbonation rates: An experimental study of the rate limiting reactions at 90 and 150 °C in open and closed systems, *Geochim. Cosmochim. Acta*, 2013, **118**, 157–183.
29 W. Xiong and D. Giammar, Forsterite Carbonation in Zones with Transport Limited by Diffusion, *Environ. Sci. Technol. Lett.*, 2014, **1**, 333–338.
30 J. S. Loring, T. E. Webb, M. E. Bowden, M. H. Engelhard and S. N. Kerisit, Cobalt substitution slows forsterite carbonation in low-water supercritical carbon dioxide, *Phys. Chem. Chem. Phys.*, 2024. DOI: 10.1039/d4cp02092h.
31 K. P. Sanosh, A. Balakrishnan, L. Francis and T. N. Kim, Sol–gel synthesis of forsterite nanopowders with narrow particle size distribution, *J. Alloys Compd.*, 2010, **495**, 113–115.
32 O. Qafoku, E. S. Ilton, M. E. Bowden, L. Kovarik, X. Zhang, R. K. Kukkadapu, M. H. Engelhard, C. J. Thompson, H. T. Schaef, B. P. McGrail, K. M. Rosso and J. S. Loring, Synthesis of nanometer-sized fayalite and magnesium-iron (II) mixture olivines, *J. Colloid Interface Sci.*, 2018, **515**, 129–138.
33 A. Saberi, B. Alinejad, Z. Negahdari, F. Kazemi and A. Almasi, A novel method to low temperature synthesis of nanocrystalline forsterite, *Mater. Res. Bull.*, 2007, **42**, 666–673.
34 S. Chen and A. Navrotsky, Calorimetric study of the surface energy of forsterite, *Am. Mineral.*, 2010, **95**, 112–117.
35 L. M. Anovitz, A. J. Rondinone, L. Sochalski-Kolbus, J. Rosenqvist and M. C. Cheshire, Nano-scale synthesis of the complex silicate minerals forsterite and enstatite, *J. Colloid Interface Sci.*, 2017, **495**, 94–101.
36 C. Zhang, R. Zuo, J. Zhang, Y. Wang and J. Jones, Structure–Dependent Microwave Dielectric Properties and Middle–Temperature Sintering of Forsterite $(Mg_{1-x}Ni_x)_2SiO_4$ Ceramics, *J. Am. Ceram. Soc.*, 2014, **98**, 702–710.
37 R. Rinaldi, G. D. Gatta, G. Artioli, K. S. Knight and C. A. Geiger, Crystal chemistry, cation ordering and thermoelastic behaviour of $CoMgSiO_4$ olivine at high temperature as studied by in situ neutron powder diffraction, *Phys. Chem. Miner.*, 2005, **32**, 655–664.
38 Y. Zheng, Y. NuLi, Q. Chen, Y. Wang, J. Yang and J. Wang, Magnesium cobalt silicate materials for reversible magnesium ion storage, *Electrochim. Acta*, 2012, **66**, 75–81.
39 M. El Hadri, H. Ahamdane and M. A. El Idrissi Raghni, Sol gel synthesis of forsterite, M-doped forsterite (M=Ni, Co) solid solutions and their use as ceramic pigments, *J. Eur. Ceram. Soc.*, 2015, **35**, 765–777.
40 M. A. Tena, R. Mendoza, C. Trobajo, J. R. García and S. García-Granda, Green and blue materials for the ceramic industry from pink $MgCo_xNi_{1-x}SiO_4$ ($0 \leq x \leq 1$) solid solutions, *Ceram. Int.*, 2023, **49**, 12021–12033.
41 P. Q. H. Nguyen, W. McKenzie, D. Zhang, J. Xu, R. Rapp, J. P. Bradley and P. Dera, Mechanochemical Synthesis of Nanocrystalline Olivine-Type Mg_2SiO_4 and $MgCoSiO_4$, *Crystals*, 2022, **12**, 369.
42 A. Hushur, M. H. Manghnani, J. R. Smyth, F. Nestola and D. J. Frost, Crystal chemistry of hydrous forsterite and its vibrational properties up to 41 GPa, *Am. Mineral.*, 2009, **94**, 751–760.
43 S. Brunauer, P. H. Emmett and E. Teller, Adsorption of Gases in Multimolecular Layers, *J. Am. Chem. Soc.*, 1938, **60**, 309–319.
44 R. C. Mahrotra, Synthesis and reactions of metal alkoxides, *J. Non-Cryst. Solids*, 1988, **100**, 1–15.
45 L. G. Hubert-Pfalzgraf, V. G. Kessler and J. Vaissermann, Soluble Ni^{II} alkoxides based on dimethylaminoisopropoxide ligands: molecular structure of $[Li(Pr^iOH)Ni(\eta^2\text{-}OR)_2Cl]_2$ and of *cis*-$NiCl_2(ROH)_2$ (R = $CHMeCH_2NMe_2$), *Polyhedron*, 1997, **16**, 4197–4203.
46 B. P. Baranwal and R. C. Mehrotra, Synthesis and characterization of some alkoxide derivatives of nickel(II), *Aust. J. Chem.*, 1980, **33**, 37–43.
47 V. Mazzini, G. Liu and V. S. J. Craig, Probing the Hofmeister series beyond water: Specific-ion effects in non-aqueous solvents, *J. Chem. Phys.*, 2018, **148**, 222805.
48 K. P. Gregory, G. R. Elliott, H. Robertson, A. Kumar, E. J. Wanless, G. B. Webber, V. S. J. Craig, G. G. Andersson and A. J. Page, Understanding specific ion effects and the Hofmeister series, *Phys. Chem. Chem. Phys.*, 2022, **24**, 12682–12718.
49 A. Rezaie, H. Ghasemi and F. Eslami, An in-depth investigation of the impact of salt nature on the formulation of microemulsion systems, *Sci. Rep.*, 2023, **13**, 14362.
50 M. V. Singh, Pyrolysis of Waste Polyolefins into Liquid Petrochemicals Using Metal Carbonate Catalyst, *Eng. Sci.*, 2022, **19**, 285–291.
51 A. F. Ferreira and A. P. Soares Dias, Pyrolysis of microalgae biomass over carbonate catalysts, *J. Chem. Technol. Biotechnol.*, 2020, **95**, 3270–3279.
52 R. Yuan and Y. Shen, Catalytic pyrolysis of biomass-plastic wastes in the presence of MgO and $MgCO_3$ for hydrocarbon-rich oils production, *Bioresour. Technol.*, 2019, **293**, 122076.

53 A. F. Gualtieri and S. Bagni, Crystal structure chemistry and color of doped-forsterites revisited by X-ray powder diffraction and UV/Vis/NIR spectroscopy, *Period. Mineral.*, 2001, **70**, 27–56.
54 M. Sassi and S. N. Kerisit, Ni and Co Incorporation in Forsterite: A Density Functional Theory Study with Hubbard Correction, *ACS Earth Space Chem.*, 2024, **8**, 1027–1038.
55 C. M. B. Henderson, S. A. T. Redfern, R. I. Smith, K. S. Knight and J. M. Charnock, Composition and temperature dependence of cation ordering in Ni-Mg olivine solid solutions: a time-of-flight neutron powder diffraction and EXAFS study, *Am. Mineral.*, 2001, **86**, 1170–1187.
56 D. Boström, Single-crystal X-ray diffraction studies of synthetic Ni-Mg olivine solid solutions, *Am. Mineral.*, 1987, **72**, 965–972.
57 M. Miyake, H. Nakamura, H. Kojima and F. Marumo, Cation ordering in Co-Mg olivine solid-solution series, *Am. Mineral.*, 1987, **72**, 594–598.
58 X. Hu, K. Langer and D. Boström, Polarized electronic absorption spectra and Ni-Mg partitioning in olivines $(Mg_{1-x}Ni_x)_2[SiO_4]$, *Eur. J. Mineral.*, 1990, **2**, 29–41.
59 S. Bock, C. Kijatkin, D. Berben and M. Imlau, Absorption and Remission Characterization of Pure, Dielectric (Nano-) Powders Using Diffuse Reflectance Spectroscopy: An End-To-End Instruction, *Appl. Sci.*, 2019, **9**, 4933.
60 K. Ullrich, O. Ott, K. Langer and K. D. Becker, Temperature dependence of the polarized electronic absorption spectra of olivines. Part II—Cobalt-containing olivines, *Phys. Chem. Miner.*, 2004, **31**, 247–260.
61 R. Newman and R. M. Chrenko, Optical Properties of Nickel Oxide, *Phys. Rev.*, 1959, **114**, 1507–1513.
62 W. Low, Paramagnetic and Optical Spectra of Divalent Nickel in Cubic Crystalline Fields, *Phys. Rev.*, 1958, **109**, 247–255.
63 A. M. Hofmeister and K. M. Pitman, Evidence for kinks in structural and thermodynamic properties across the forsterite–fayalite binary from thin-film IR absorption spectra, *Phys. Chem. Miner.*, 2007, **34**, 319–333.
64 V. E. Hamilton, Thermal infrared (vibrational) spectroscopy of Mg–Fe olivines: A review and applications to determining the composition of planetary surfaces, *Geochemistry*, 2010, **70**, 7–33.
65 P. S. Bagus, C. J. Nelin, C. R. Brundle, B. V. Crist, E. S. Ilton, N. Lahiri and K. M. Rosso, Main and Satellite Features in the Ni 2p XPS of NiO, *Inorg. Chem.*, 2022, **61**, 18077–18094.
66 W. He, X. Li, S. An, T. Li, Y. Zhang and J. Cui, 3D β-$Ni(OH)_2$ nanowires/RGO composite prepared by phase transformation method for superior electrochemical performance, *Sci. Rep.*, 2019, **9**, 10838.
67 Z. Zhao, N. Lakshminarayanan, S. L. Swartz, G. B. Arkenberg, L. G. Felix, R. B. Slimane, C. C. Choi and U. S. Ozkan, Characterization of olivine-supported nickel silicate as potential catalysts for tar removal from biomass gasification, *Appl. Catal., A*, 2015, **489**, 42–50.
68 H. Ming and B. G. Baker, Characterization of cobalt Fischer-Tropsch catalysts I. Unpromoted cobalt-silica gel catalysts, *Appl. Catal., A*, 1995, **123**, 23–36.
69 P. Guo and C. Wang, Synthesis and lithium storage performance of Co_2SiO_4 nanoparticles, *RSC Adv.*, 2015, **5**, 70661–70667.
70 Y. Okamoto, K. Nagata, T. Adachi, T. Imanaka, K. Inamura and T. Takyu, Preparation and Characterization of Highly Dispersed Cobalt Oxide and Sulfide Catalysts Supported on SiO_2, *J. Phys. Chem.*, 1991, **95**, 310–319.
71 H. W. Nesbitt, D. Legrand and G. M. Bancroft, Interpretation of Ni2p XPS spectra of Ni conductors and Ni insulators, *Phys. Chem. Miner.*, 2000, **27**, 357–366.
72 P. H. Tewari and W. Lee, Adsorption of Co(II) at the oxide-water interface, *J. Colloid Interface Sci.*, 1975, **52**, 77–88.
73 C. V. Schenck, J. G. Dillard and J. W. Murray, Surface analysis and the adsorption of Co(II) on goethite, *J. Colloid Interface Sci.*, 1983, **95**, 398–409.
74 K. S. Kim, X-ray-photoelectron spectroscopic studies of the electronic structure of CoO, *Phys. Rev. B*, 1975, **11**, 2177–2185.
75 V. P. Zakaznova-Herzog, H. W. Nesbitt, G. M. Bancroft and J. S. Tse, Characterization of leached layers on olivine and pyroxenes using high-resolution XPS and density functional calculations, *Geochim. Cosmochim. Acta*, 2008, **72**, 69–86.
76 E. Talik, W. Zarek, M. Kruczek, S. Ganschow, D. Skrzypek and E. Popiel, Characterization of olivine single crystals grown by the micro–pulling–down method and terrestrial olivine by XPS, Mössbauer, magnetic and EPR methods, *Cryst. Res. Technol.*, 2006, **41**, 979–987.

